Low-Temperature Fabrication of Efficient Wide-Bandgap Organolead Trihalide Perovskite Solar Cells

*Cheng Bi, Yongbo Yuan, Yanjun Fang, and Jinsong Huang**

To exceed the Shockley–Queisser efficiency limit, tandem solar cell devices with complementary absorption spectra is needed to increase the absorption of sunlight over a wide range of wavelengths while minimizing thermodynamic loss in individual cells. Crystalline-Si (c-Si) technology produces excellent single-junction solar cells with power conversion efficiencies (PCEs) of 24%–25%, and has been commercialized extensively to produce panels at relatively low costs, but it has not become competitive yet with nonrenewable energy sources. Enhanced device performance is still required to reduce the price of solar electricity to below \$0.06 (kW h)$^{-1}$ so that photovoltaics become a cost effective solution as a standard electricity source. To produce efficient tandem cell with c-Si, a material is needed that can be deposited inexpensively on c-Si and has a bandgap matched with c-Si in tandem cells. To match the bandgap of c-Si (1.12 eV), a material with bandgap of 1.72 eV is needed to produce a short-circuit current density (J_{SC}) of ≈20 mA cm^{-2} under air mass (AM) 1.5 spectrum, which can potentially produce high device efficiency above 30%.[1,2] These requirements can be met by using the organometal trihalide perovskite materials.

Organometal trihalide perovskite are nature abundant, solution processable, low-cost materials that have been converted to efficient single-junction photovoltaic devices with power conversion efficiency above 15%.[3–6] Similar to silicon solar cells, the intrinsic voltage loss in perovskite solar cells is among the lowest. It is therefore most promising to combine these two types of most efficient solar cells to boost the device efficiency without significantly adding device fabrication cost. However, it is not feasible to directly apply the developed high efficiency single-junction perovskite solar cells onto silicon solar cells for tandem devices due to the following two reasons: 1) the optical bandgap of the perovskites in most efficient perovskite solar cells is 1.55 eV that is still too small to match the bandgap of Si solar cells in tandem devices; 2) most of these devices use mesoporous titanium oxide as electron extraction layers, which were formed at high temperature above 400 °C for the best device performance.[5,6] The high-temperature process can dramatically degrade the bottom silicon cells.

In this paper, we demonstrate a high performance mixed halide perovskite photovoltaic device with an enlarged bandgap of 1.72 eV fabricated by a low-temperature solution process (100 °C). An efficiency of 13.1%, which is the highest reported efficiency for wide-bandgap perovskite solar cells to the best of our knowledge, was achieved by carefully tuning the thickness, morphology, and surface passivation of the perovskite layers. These fabrication techniques and conditions are compatible with the bottom silicon cells for future tandem cell application.

One merit of the hybrid organometal trihalide perovskite materials for photovoltaic application is its bandgap can be favorably tuned between 1.17 and 3.11 eV by incorporating varied halide (Cl, Br, and I), metal and organic ions.[5,7–16] In this work, we tuned the bandgap of the perovskite to 1.72 eV using mixed halide perovskite of $CH_3NH_3PbI_{3-x}Br_x$ ($MAPbI_{3-x}Br_x$). For the $MAPbI_{3-x}Br_x$ film formation, lead iodine (PbI_2) layers were first spun on the indium tin oxide (ITO)/poly(3,4-ethylenedioxythiophene) poly(styrenesulfonate) substrates from dimethylformamide (DMF) solution, and then CH_3NH_3Br (MABr):CH_3NH_3I (MAI) blended precursor solution with different blend ratios were spun onto the PbI_2 layers. The continuous and pinhole-free $MAPbI_{3-x}Br_x$ films were formed by the annealing-driven interdiffusion process, while I and Br were spontaneously incorporated into the mixed halide perovskites, as shown in **Figure 1**a. Detailed film and device fabrication process can be found in the experimental section. The perovskite's bandgap can be tuned by varying MABr percentage in the blended precursor solution. Here, 150 nm thick PbI_2 layers were used to react with MABr:MAI blended solution containing different MABr:MAI ratio. The absorption spectra of as-fabricated perovskite films in Figure 1b shows a continuous blue shift of the absorption cut-off edge with increased Br percentage ratio in the precursor blend. The optical bandgap (Eg), which was shown as an inset in Figure 1b, has a nearly linear relationship with molar percentage of Br with as relationship of Eg (eV) = 1.54 + 0.294y, where y is the molar percentage of MABr in the MABr:MAI precursor solution. The absorption edge was shifted to 676 nm when pure MABr solution was used, and a bandgap of 1.72 eV was obtained by blending 56.3 mol% MABr into the precursor. By assuming a linear relationship of Br incorporation with the bandgap of $MAPbI_{3-x}Br_x$, we derived a composition of $MAPbI_{2.4}Br_{0.6}$ for the mixed halide perovskite that has a bandgap of 1.72 eV. In our previous study of Cl incorporation into $MAPbI_3$ by interdiffusion, it was found the Cl incorporation involved two steps: first formation of Cl-rich perovskite phase dispersed in $MAPbI_3$ before thermal annealing, and then homogenization of the two phases to one single phase after thermal annealing.[17] It can be explained by low formation energy of Cl-rich perovskite. Here, it is found that the film's optical bandgap did not change before and after thermal annealing-induced diffusion process, as shown in Figure 1c, indicating the Br in perovskite has the comparable

C. Bi, Dr. Y. Yuan, Dr. Y. Fang, Prof. J. Huang
Department of Mechanical & Materials Engineering and Nebraska Center for Materials and Nanoscience
University of Nebraska-Lincoln
Lincoln, NE 68588-0656, USA
E-mail: jhuang2@unl.edu

DOI: 10.1002/aenm.201401616

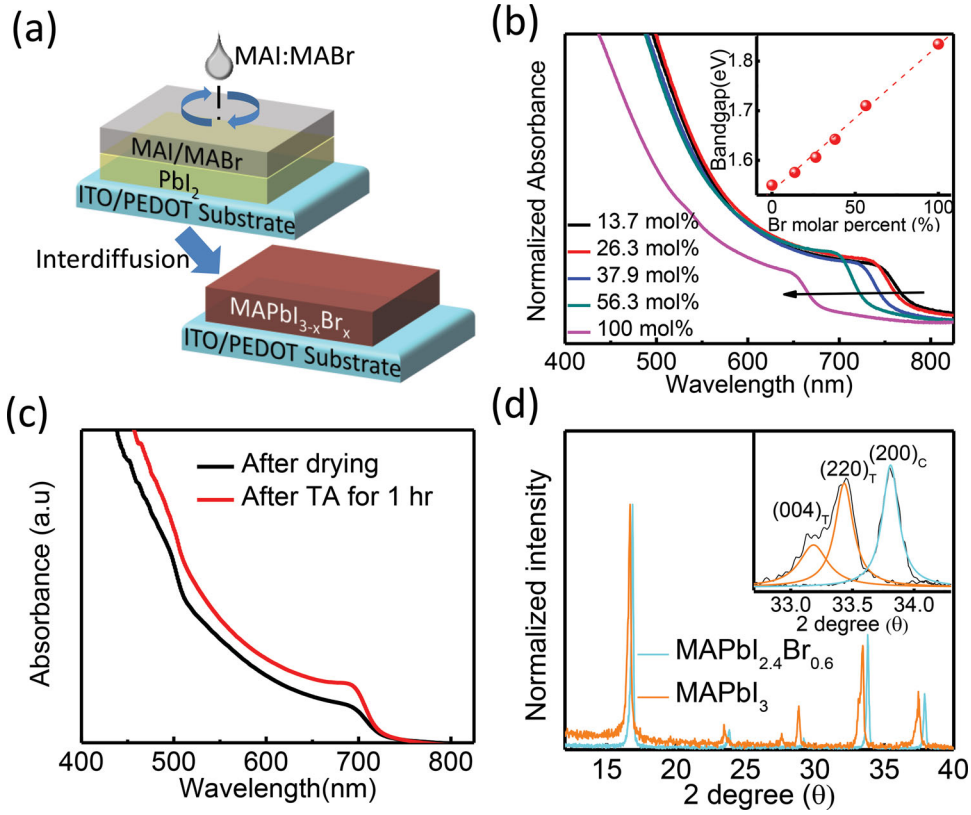

Figure 1. a) The schematic of fabricating $MAPbI_{3-x}Br_x$ film by using two stacked precursor layers; b) optical absorption of films grown from varied MABr percent in the MABr:MAI blended precursor solution, and the inset figure showing the linear correlation of bandgap to MABr percent in blended solution; c) absorption of the $MAPbI_{2.4}Br_{0.6}$ films after drying and thermal annealing; d) XRD pattern of $MAPbI_{2.4}Br_{0.6}$ and $MAPbI_3$ film, and magnified region showing $(004)_T$, $(220)_T$, and $(200)_C$ peak in the inserted figure.

incorporation rate with I. The increased absorbance after the annealing suggests that although Br can be readily incorporated even at room temperature, a thermal annealing at 100 °C is still needed to drive the interdiffusion of two stacking precursor layers into each other to complete the reaction.

The interdiffusion grown $MAPbI_{2.4}Br_{0.6}$ film was studied by X-ray diffraction (XRD) measurement to confirm the incorporation of Br in to the lattice of $MAPbI_3$. Figure 1(d) shows the XRD pattern of the $MAPbI_{2.4}Br_{0.6}$ film annealed for 80 min, and the XRD pattern of a $MAPbI_3$ film was also shown for comparison. All the XRD peaks of the $MAPbI_{2.4}Br_{0.6}$ film shifted to larger diffraction angles, and only one single phase exists, indicating the successful incorporation of Br into $MAPbI_3$ after interdiffusion process. It is also found that the Br incorporation transferred the perovskite crystal from tetragonal structure to cubic structure, because the (004) peak at 33.17° in $MAPbI_3$ disappeared in XRD pattern of $MAPbI_{2.4}Br_{0.6}$, as shown in the inserted pattern in Figure 1d.[7,8] The lattice constant of $MAPbI_{2.4}Br_{0.6}$ was calculated to be 0.617 nm, agreeing with the previously reported value of $MAPbI_{3-x}Br_x$ with a same bandgap.[7] The relative intensity of different diffraction peaks of the $MAPbI_{2.4}Br_{0.6}$ films had negligible change, suggesting Br incorporation caused no preferred grain orientation, which is again different from that of Cl incorporation into $MAPbI_3$. The difference can be explained by the similar atom size of Br with I, while Cl has much smaller size than I.

After determining the composition for a proper bandgap, we continue to improve the morphology of the $MAPbI_{2.4}Br_{0.6}$ films for high-efficiency devices. To get a high-performance photovoltaic device, a proper thickness for the perovskite layer is needed to absorb most of light for maximum charge generation. For $MAPbI_{2.4}Br_{0.6}$ perovskite, a film thicker than 600 nm is required to absorb above 90% light in its whole absorption spectrum region, as can be derived from the thickness-dependent absorption curves shown in **Figure 2**a. Nevertheless, a too thick active layer always increases the chance of charge recombination, reducing charge collection efficiency. Charge recombination is generally associated with defects in crystals. Recent theoretical calculations by Hong and co-workers and Yin et al.[18–20] revealed that this unique family of materials is tolerant to point defects because the point defects do not generate trap states in the bandgap, explaining the very large charge diffusion length in organometal trihalide perovskites. However, the grain boundaries can cause severe charge recombination due to nonstoichimometric composition at grain boundaries. Our previous study showed that grain boundaries can lose MAI during thermal annealing, and generates a high density of charge traps.[21,22] Therefore, large crystalline grains are preferred to minimize the charge recombination in the thick $MAPbI_{2.4}Br_{0.6}$ film. However, we found it difficult to grow large $MAPbI_{2.4}Br_{0.6}$ grains by thermal annealing. The average gain size of $MAPbI_{2.4}Br_{0.6}$ is limited to be around 300–350 nm even after extended thermal

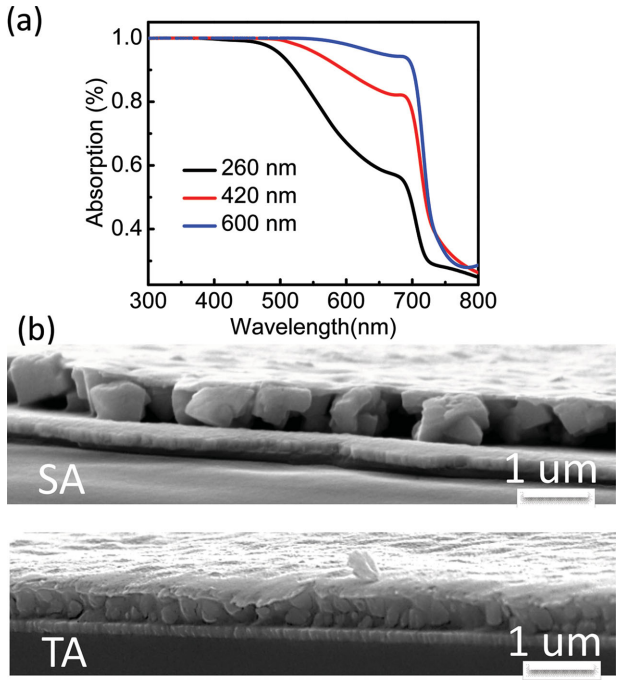

Figure 2. a) Thickness-dependent absorption of $MAPbI_{2.4}Br_{0.6}$ film; b) cross-section SEM images of 600 nm thick $MAPbI_{2.4}Br_{0.6}$ devices with solvent (SA) and thermal (TA) annealed perovskite film.

annealing to 2 h, while further increasing annealing temperature would pose risk of obvious perovskite decomposition.[23,24] Therefore, we adopted a solvent assisted thermal annealing method to boost the grain size. DMF, which is a good solvent for all the precursors, was added into the annealing atmosphere to assist the grain grown.[25] Here, a controlled film with only thermal annealing was also included for comparison to demonstrate the effect of solvent annealing in $MAPbI_{2.4}Br_{0.6}$ films. Figure 2b shows the cross-section scanning electron microscopy (SEM) images of the devices fabricated from thermal- and solvent-annealed $MAPbI_{2.4}Br_{0.6}$ films with a thickness of 600 nm. It clearly shows that thermal-annealing produced small grains with average size of around 300 nm, while solvent annealing yielded large grains with size comparable to or larger than the film's thickness, which allows charge carriers transport in a single grain without encountering grain boundary before being collected. A decrease of total charge recombination is expected from the significant reduction of total boundary area, which can result in more efficient charge collection for an improved photocurrent and fill factor (FF), which was demonstrated in the device performance study.

We fabricated devices with different $MAPbI_{2.4}Br_{0.6}$ thickness with a planar device structure of ITO/PEDOT:PSS/$MAPbI_{2.4}Br_{0.6}$/phenyl-C61-butyric acid methyl ester (PCBM) (20 nm)/C_{60} (20 nm)/2,9-dimethyl-4,7-diphenyl-1,10-phenanthroline (BCP)(8 nm)/aluminum (100 nm), as shown in **Figure 3**a. Figure 3b shows the photocurrent density–voltage (J–V) curves of best performing $MAPbI_{2.4}Br_{0.6}$ devices with varied thicknesses from 260 to 600 nm. To examine the effect of solvent annealing on device performance, the photocurrent of the best thermal-annealed 420 nm thick $MAPbI_{2.4}Br_{0.6}$ device was also

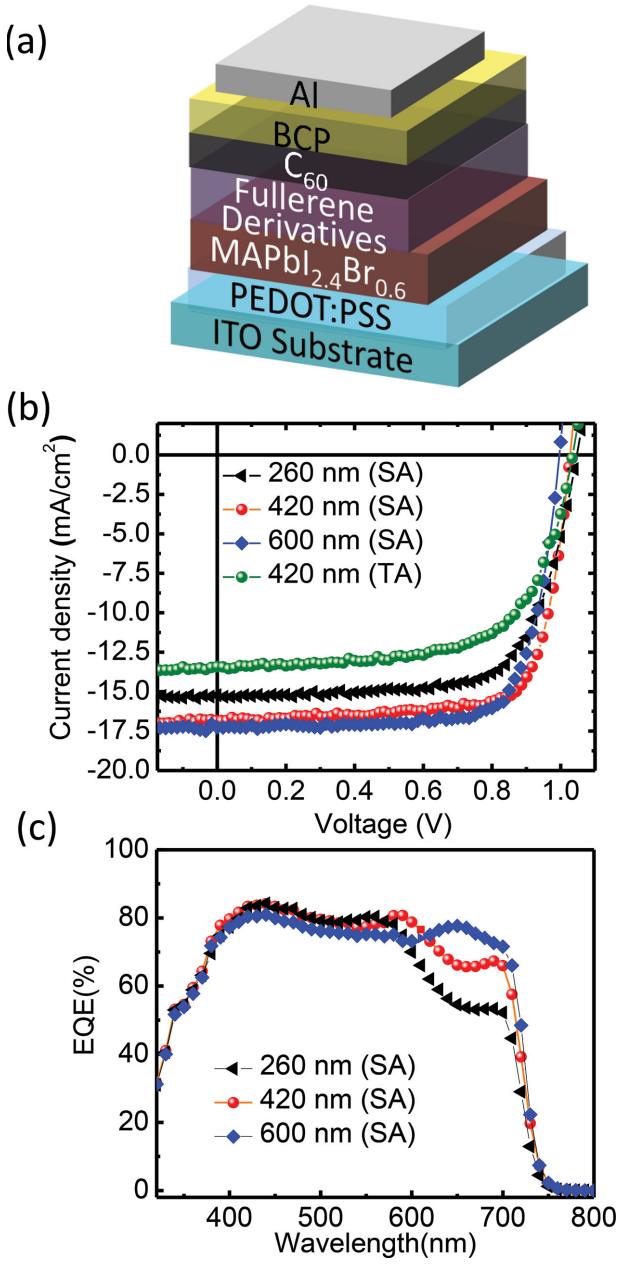

Figure 3. a) The schematic of $MAPbI_{2.4}Br_{0.6}$ photovoltaic device structure; b) J–V curve and c) EQE of the devices with varied $MAPbI_{2.4}Br_{0.6}$ film thickness. TA and SA in the figure mean thermal and solvent-annealing treatment for the perovskite film, respectively.

shown in the Figure 3b. Clearly, the thermal-annealed films yielded lower J_{SC} and FF than the solvent-annealed films, which can be explained by the stronger charge recombination due to the larger grain boundary area in thermal-annealed films. Increasing the $MAPbI_{2.4}Br_{0.6}$ film thickness to 600 nm produced a larger J_{SC} of 17.3 mA cm^{-2}, as compared with 15.2 mA cm^{-2} from 260 nm thick film device. It can be explained by the stronger absorption in the long wavelength range between 600 and 750 nm, as proven by the absorption curves in Figure 2a of the films and EQE curves of these devices at Figure 3c. The maximum EQE was above 80.0% for

Table 1. Film thickness-dependent performance for the device of ITO/PEDOT: PSS/$MAPbI_{2.4}$ $Br_{0.6}$/ PCBM/C_{60}/BCP/Al. TA and SA in the table mean thermal- and solvent-annealing treatment for the perovskite film, respectively.

Thickness [nm]	J_{SC} [mA cm^{-2}]	V_{OC} [V]	FF [%]	PCE [%] average	PCE [%] best
260(SA)	14.7 ± 0.7	1.04 ± 0.2	68.2 ± 2.7	10.5 ± 0.7	11.2
420(SA)	16.7 ± 0.8	1.02 ± 0.2	70.9 ± 4.8	12.0 ± 1.1	13.1
600(SA)	16.8 ± 0.7	1.01 ± 0.2	71.5 ± 4.0	11.9 ± 1.1	13.0
420(TA)	13.0 ± 0.5	1.04 ± 0.2	62.5 ± 3.8	8.4 ± 0.7	9.1

all the devices with different thickness, indicating the devices have excellent charge collection efficiency and negligible charge recombination. All EQE curves have a cutoff around 720 nm, confirming the bandgap of 1.72 eV. Increasing the thickness of $MAPbI_{2.4}Br_{0.6}$ was also found to increase the FF from 70.6% to 75.5%, but reduce open-circle voltage (V_{OC}) from 1.04 to 1.00 V. Devices with both 420 and 600 nm thick films showed comparable good performance with power convert efficiency of 13.0%. The thickness-dependent device efficiency was summarized in **Table 1** for both the best and the average devices. The average efficiency of the 420 and 600 nm thick devices treated by solvent annealing reached 12.0% and 11.9%, respectively, while devices with 260 nm film generally yielded a lower average efficiency of 10.5%. The device performances and their variations are summarized in Table 1. The insensitivity of PCE to perovskite film thickness between 420 and 600 nm relieves the requirement of accurate thickness controlling, and thus benefits the device fabrication yield.

One unique structure of our planar heterojunction device is that a layer of spun fullerene derivatives on the top of perovskite layers was introduced in addition to the thermal evaporated C_{60} layer.[21] It was found PCBM had additional passivation effect on grain boundary and film surface in $MAPbI_3$ devices because inserting PCBM was found to further reduce the total trap densities and eliminate the photocurrent hysteresis.[22] Since, it is not clear if any other fullerene derivatives have better passivation effect on $MAPbI_{2.4}Br_{0.6}$ device or the varied energy level of fullerene derivatives would impact the electron transfer from $MAPbI_{2.4}Br_{0.6}$ to them, in this study varied fullerene layers including PCBM, indene-C_{60} tri-adducts (ICTA) and indene-C_{60} bisadduct (ICBA) were tested in 420 nm thick $MAPbI_{2.4}Br_{0.6}$ devices to examine their influence. **Figure 4**a–d shows the *J–V* curves of the devices using different spun fullerene derivative layers under increasing and decreasing applied bias. The photocurrents were measured at a rate of 0.06 V min^{-1} under AM 1.5 illumination. It was found that both PCBM and ICTA can effectively passivate the $MAPbI_{2.4}Br_{0.6}$ films, resulting a PCE larger than 12.0%, J_{SC} of 17.5 mA cm^{-2} and FF of 70.0%, while ICBA or no spun fullerene passivation overall yielded a lower PCE with smaller J_{SC}, reduced FF and significant decreased V_{OC}. Nevertheless, it is noted that only PCBM passivated device showed no photocurrent hysteresis when changing the photocurrent sweep directions, while the device with ICTA, although showed a similar PCE as compared with PCBM device under increasing applied bias, was observed to have photocurrent hysteresis with lower J_{SC} and FF when changing the photocurrent

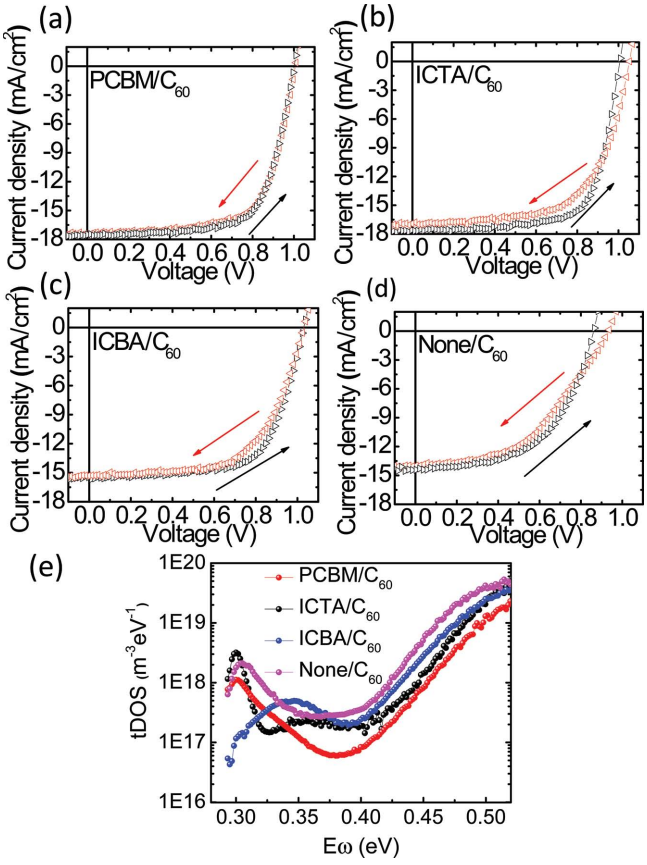

Figure 4. a–d) *J–V* curve and e) *t*DOS of the $MAPbI_{2.4}Br_{0.6}$ devices with PCBM, ICTA, ICBA, and without fullerene derivative passivation, respectively.

sweep direction. The similar observation was also found in the devices with ICBA and no fullerene. The devices' performance measured with forward and reverse sweep direction is summarized in **Table 2**. The observed photocurrent hysteresis may come from the insufficient passivation on charge traps in $MAPbI_{2.4}Br_{0.6}$ perovskite films.[21,22] To investigate the varied fullerene derivatives' passivation effect on grain boundary and surface traps, we used thermal admittance spectroscopy (TAS) to measure the trap density of states (*t*DOS) in these devices. TAS is well-established technique for *t*DOS measurement for thin film solar cells.[21,22,26,27] Figure 4e shows the *t*DOS for the devices with different fullerene derivatives. It is observed that the device with PCBM had overall the lowest *t*DOS over the whole region, explaining the least photocurrent hysteresis in these devices. The device with ICTA had 2–3 times larger *t*DOS in the shallow trap region of 0.34–0.40 eV, 75%–100% larger *t*DOS in deeper trap region (0.40–0.52 eV) than that of the device with PCBM. In addition, the devices with ICBA and no spun derivative overall have much higher *t*DOS, especially in deep trap region. The low device efficiency and observed photocurrent hysteresis can be explained by the higher *t*DOS. In our previous study, we already established the shallow traps were mainly passivated by spun fullerene derivatives because they can diffuse into grain boundaries under thermal annealing, while deep traps at perovskite surface were passivated by both

Table 2. Performance of the devices passivated by varied fullerene derivatives (ITO/PEDOT: PSS/$MAPbI_{2.4}Br_{0.6}$/fullerene derivatives/C_{60}/BCP/Al).

Fullerene derivatives	J_{SC} [mA cm^{-2}] forward/reverse	V_{OC} [V] forward/reverse	FF [%] forward/reverse	PCE [%] forward/reverse
PCBM/C_{60}	17.5/17.5	1.00/1.01	70.0/68.1	12.2/12.0
ICTA/C_{60}	17.5/17.1	1.01/1.05	70.9/62.5	12.5/11.2
ICBA/C_{60}	15.4/15.3	1.02/1.02	66.9/61.2	10.5/9.6
None/C_{60}	14.4/14.0	0.87/0.94	54.4/46.9	6.8/6.1

spun fullerene derivative and C_{60}. The varied passivation capability by these different fullerene derivatives to $MAPbI_{2.4}Br_{0.6}$ possibly originated from the different penetrating ability of the fullerene derivatives into the grain boundaries, and the selective passivation of charge traps with different energy levels. This result clearly proves that, the trap states in $MAPbI_{2.4}Br_{0.6}$ can also be efficiently passivated by PCBM, despite of the broadened bandgap.

The best performing device was obtained using PCBM passivation on a 420 nm thick perovskite film. A PCE of 13.1% was achieved with J_{SC} of 17.5 mA cm^{-2}, V_{OC} of 1.02 V and FF of 73.7%, as shown in **Figure 5**a. This J_{SC} is close to the ideal value of 20 mA cm^{-2} so that the photocurrent of the perovskite cell and Si cell can match with each other. The EQE curve in Figure 5b shows that the maximum EQE reached 84.8% at 530 nm, and was above 80.0% in the wavelength range of 470–650 nm. It should be noted that the ITO substrate used here is different from those used in the study of perovskite thickness-dependent device performance. The ITO in this highest efficiency device had less transparency in blue region, causing a slight reduction of EQE between 400 and 475 nm. One can infer that the transparency of ITO substrate could have non-negligible impact photovoltaic device efficiency, and thus the further device optimization should also include the improvement of light harvesting.

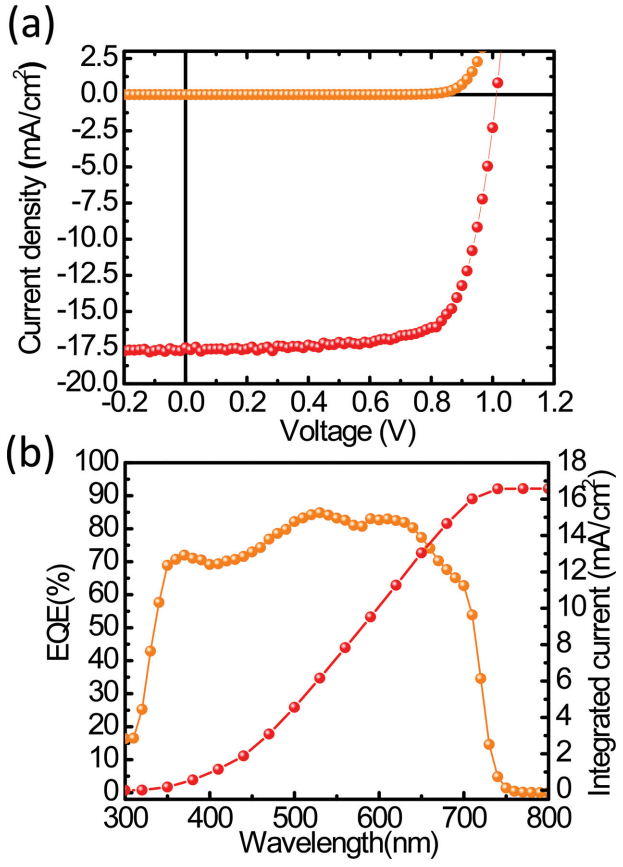

Figure 5. a) *J–V* curve and b) EQE of the best performing device.

In summary, a high performance perovskite photovoltaic device with 1.72 eV bandgap was developed by a low-temperature solution process for Si/perovskite tandem solar cell. Hybrid halide was used to enlarge the bandgap by precise control of Br incorporation into perovskite to obtain 1.72 eV bandgap that was optimized for a most efficient Si/perovskite tandem solar cell. The optimized thickness of perovskite layer was between 420 and 600 nm that is thicker than that of the reported most efficient $MAPbI_3$ devices. Solvent annealing was used to grow large grains so grain size can reach the thickness of the perovskite layer even for thick films, which significantly reduced charge recombination and improved device performance. PCBM passivation was found necessary to achieve the optimized device with a PCE of 13.1%. The low-temperature processed, high efficiency, large bandgap perovskite solar cells developed in this work have potential to be integrated with Si solar cell for high efficient silicon/perovskite tandem devices.

Experimental Section

Material Synthesis and Perovskite Film Formation: The MAI was synthesized by following the method reported in other literature.[28] For the film fabrication, a PbI_2 layer was firstly spun onto the top of ITO substrate at a spin rate of 6000 rpm from a hot PbI_2 DMF solution (100 °C). To obtain varied thick $MAPbI_{2.4}Br_{0.6}$ film, the PbI_2 layers were prepared from precursor solutions with different concentration: 400, 600, and 800 mg mL^{-1} PbI_2 DMF solutions were used for 260, 420, and 600 nm $MAPbI_{2.4}Br_{0.6}$ film, respectively. The as-prepared PbI_2 film was dried in a hotplate at 100 °C for 5 min and then a MAI: MABr layer was spun coated on the top of the PbI_2 layer at a spin rate of 6000 rpm for 35 s. To obtain the expected bandgap of 1.72 eV, an optimized concentration of MAI: MABr solution with a specific blend ratio was used. 40 mg mL^{-1} blended solution with 47.5 wt% MABr, 60 mg mL^{-1} blended solution with 50 wt% MABr, and 80 mg mL^{-1} blended solution with 50 wt% MABr were used to fabricate 260, 420, and 600 nm $MAPbI_{2.4}Br_{0.6}$ films, respectively. The stacked two precursor layers were then dried at 70 °C for 5 min and sequently annealed at 100 °C for 80 min. The films were placed in a hot plate with a cover of a glass petri dish during annealing. To apply solvent annealing, 8 µL DMF solvent was added to the edge of the petri dish when the annealing started. The solvent annealing process was taken in 100 °C for 80 min.

Device Fabrication: After annealing, a layer of PCBM was spun on the prepared perovskite film from a 20 mg mL^{-1} dichlorobenzene solution at a spin rate of 6000 rpm for 35 s and then the film was thermally annealed for 1 h at 100 °C. To prepare the samples with varied fullerene derivatives for passivation effect study, ICTA and ICBA layers were prepared in exactly the same way. To finish the device fabrication, 20 nm C_{60}, 8 nm BCP, and 100 nm Al electrode were sequentially deposited by thermal evaporation. The device area was 7.5 mm^2 and was defined by the overlap of the Al electrode with the film and anode. All the film fabrication was processed in nitrogen-filled glovebox.

Film Characterization: Evolution 201 UV-Visible spectrometer (thermo Scientific) was used to measure the absorption spectra of the perovskite films. A Rigaku D/Max-B X-ray diffractometer with Bragg–Brentano parafocusing geometry was used to obtain the XRD patterns. The diffractometer had a Co–Kα tube with emitted wavelength of 1.79 Å. The cross-section SEM images were taken by a Quanta 200 FEG environmental SEM.

Device Characterization: Device's *J–V* measurement was performed under the simulated AM 1.5G irradiation (100 mW cm^{-2}) from a Xenon-lamp-based solar simulator (Oriel 67005, 150 W Solar Simulator), and a Si diode (Hamamatsu S1133) equipped with a Schott visible-color glass-filtered (KG5 color-filtered) was used to calibrate the light intensity. Keithley model 2400 was used for current-voltage measurement. LCR (inductance (*L*), capacitance (*C*), and resistance (*R*)) meter (Agilent E4980A) was used to perform TAS measurement for the devices' *t*DOS derivation. The devices' *t*DOS was derived from angle frequency-dependent capacitance and voltage-dependent capacitance based on the equation: $N_T(E_\omega) = -\frac{V_{bi}}{qW}\frac{dC}{d\omega}\frac{\omega}{k_B T}$, where ω, C, q, k_B, and T are the angular frequency, capacitance, elementary charge, Boltzmann's constant, and absolute temperature, respectively. V_{bi} and W are the built-in potential and depletion width, and can be derived from voltage-dependent capacitance. The angular frequency ω was defined by the equation: $E_\omega = k_B T \ln\left(\frac{\omega_0}{\omega}\right)$, where ω_0 is the attempt-to-escape frequency.

Acknowledgements

J.H. thanks the financial support from the Department of Energy under Award DE-EE0006709.

Received: September 12, 2014
Revised: October 20, 2014
Published online: November 25, 2014

[1] J. C. Fan, B.-Y. Tsaur, B. Palm, presented at *Phot. Spec. Conf.* San Diego, September **1982**.
[2] T. Soga, T. Kato, M. Yang, M. Umeno, T. Jimbo, *J. Appl. Phys.* **1995**, *78*, 4196.
[3] M. Liu, M. B. Johnston, H. J. Snaith, *Nature* **2013**, *501*, 395.
[4] K. Wojciechowski, M. Saliba, T. Leijtens, A. Abate, H. J. Snaith, *Energy Environ. Sci.* **2014**, *7*, 1142.
[5] N. J. Jeon, J. H. Noh, Y. C. Kim, W. S. Yang, S. Ryu, S. I. Seok, *Nat. Mater.* **2014**, *13*, 897.
[6] J. Burschka, N. Pellet, S.-J. Moon, R. Humphry-Baker, P. Gao, M. K. Nazeeruddin, M. Gratzel, *Nature* **2013**, *499*, 316.
[7] J. H. Noh, S. H. Im, J. H. Heo, T. N. Mandal, S. I. Seok, *Nano Lett.* **2013**, *13*, 1764.
[8] S. Aharon, B. E. Cohen, L. Etgar, *J. Phys. Chem. C* **2014**, *118*, 17160.
[9] B. Suarez, V. Gonzalez-Pedro, T. S. Ripolles, R. S. Sanchez, L. Otero, I. Mora-Sero, *J. Phys. Chem. Lett.* **2014**, *5*, 1628.
[10] S. Ryu, J. H. Noh, N. J. Jeon, Y. Chan Kim, W. S. Yang, J. Seo, S. I. Seok, *Energy Environ. Sci.* **2014**, *7*, 2614.
[11] Y. Ogomi, A. Morita, S. Tsukamoto, T. Saitho, N. Fujikawa, Q. Shen, T. Toyoda, K. Yoshino, S. S. Pandey, T. Ma, S. Hayase, *J. Phys. Chem. Lett.* **2014**, *5*, 1004.
[12] N. Kitazawa, Y. Watanabe, Y. Nakamura, *J. Mater. Sci.* **2002**, *37*, 3585.
[13] J. Qiu, Y. Qiu, K. Yan, M. Zhong, C. Mu, H. Yan, S. Yang, *Nanoscale* **2013**, *5*, 3245.
[14] B. Cai, Y. Xing, Z. Yang, W.-H. Zhang, J. Qiu, *Energy Environ. Sci.* **2013**, *6*, 1480.
[15] Y. Zhao, K. Zhu, *J. Am. Chem. Soc.* **2014**, *136*, 12241.
[16] P.-W. Liang, C.-C. Chueh, X.-K. Xin, F. Zuo, S. T. Williams, C.-Y. Liao, A. K.-Y. Jen, *Adv. Energy Mater.* **2014**, DOI: 10.1002/aenm.201400960.
[17] Q. Dong, Y. Yuan, Y. Shao, Y. Fang , J. Huang, unpublished.
[18] J. Kim, S.-H. Lee, J. H. Lee, K.-H. Hong, *J. Phys. Chem. Lett.* **2014**, *5*, 1312.
[19] W.-J. Yin, T. Shi, Y. Yan, *Appl. Phys. Lett.* **2014**, *104*, 063903.
[20] W.-J. Yin, T. Shi, Y. Yan, *Adv. Mater.* **2014**, *26*, 4653.
[21] Q. Wang, Y. Shao, Q. Dong, Z. Xiao, Y. Yuan, J. Huang, *Energy Environ. Sci.* **2014**, *7*, 2359.
[22] Y. Shao, Z. Xiao, C. Bi, Y. Yuan, J. Huang, *Nat. Commun.* **2014**, *5*, 5784.
[23] A. Dualeh, N. Tétreault, T. Moehl, P. Gao, M. K. Nazeeruddin, M. Grätzel, *Adv. Funct. Mater.* **2014**, *24*, 3250.
[24] C. Bi, Y. Shao, Y. Yuan, Z. Xiao, C. Wang, Y. Gao, J. Huang, *J. Mater. Chem. A*, **2014**, *2*, 18508.
[25] Z. Xiao, Q. Dong, C. Bi, Y. Shao, Y. Yuan, J. Huang, *Adv. Mater.* **2014**, *26*, 6503.
[26] T. Walter, R. Herberholz, C. Müller, H. W. Schock, *J. Appl. Phys.* **1996**, *80*, 4411.
[27] C. Melzer, E. J. Koop, V. D. Mihailetchi, P. W. M. Blom, *Adv. Funct. Mater.* **2004**, *14*, 865.
[28] M. M. Lee, J. Teuscher, T. Miyasaka, T. N. Murakami, H. J. Snaith, *Science* **2012**, *338*, 643.